

Deliverable D2.2

Database for thermal effects on microstructure and mechanical properties of DILAFACT materials

Funded by the European Union. Views and opinions expressed are however those of the author(s) only and do not necessarily reflect those of the European Union. Neither the European Union nor the granting authority can be held responsible for them.

Copyright © by DILAPRO All Rights Reserved

Revision	Date	Author/Organisation	Description
1	28/02/25	IMDEA	Concept of the Deliverable
2	09/04/25	IMDEA, DTI, DTU, DCU, CRM and Prima Additive	Draft
3	28/04/25	IMDEA, DTI, DTU, DCU, CRM and Prima Additive	Revised
4	29/07/25	IMDEA, DTI, DTU, DCU, CRM and Prima Additive	Revised



Action number: #101138859

Action Acronym: DILAPRO
Action Name: Digital Laser Production

Deliverable Due date: 30/04/25
Deliverable hand-in date (Vs2): 31/07/25

Copyright © by DILAPRO All Rights Reserved | D2.2 – Database for thermal effects on microstructure and mechanical properties of DILAFACT materials

Table of contents

1. List of abbreviations 3

2. Executive Summary 4

3. Effect of process parameters and heat treatments on the microstructure and mechanical properties 5

3.1 Stainless steel 316L 5

3.2 Inconel 718 13

3.3 Inconel 625 18

4. General conclusions 26

5. Bibliography 27

Copyright © by DILAPRO All Rights Reserved

1. List of abbreviations

AM	Additive Manufacturing
AMS	Aerospace Material Specifications
ASME	American Society of Mechanical Engineering
ASTM	American Society for Testing and Materials
BD	Building Direction
BOP	Blow Out Preventer
BSD	Backscatter Detector
DLD	Direct Laser Deposition
DSM	Double Stagger Melt
EBSD	Electron Backscatter Diffraction
EDM	Electrical Discharge Machining
EDS	Energy Dispersive Spectroscopy
GB	Grain Boundary
GMA	Gas Metal Arc
GND	Geometrically Necessary Dislocations
HAADF	High-Angle Annular Dark Field
HAGB	High Angle Grain Boundaries
HB	Hardness Brinell
HRTEM	High Resolution Transmission Electron Microscopy
IN	Inconel
IPF	Inverse Pole Figure
IQ	Image Quiality
KAM	Kernel Average Misorientation
LAGB	Low Angle Grain Boundaries
LBM	Laser Beam Melting
LC	Laser Consolidation
LENS	Laser Engineered Net Shaping
LPBF	Laser Powder Bed Fusion
LRM	Laser Rapid Manufacturing
OM	Optical Microscopy
SE	Secondary Electron
SEM	Scanning Electron Microscopy
SLM	Selective Laser Melting
SS	Stainless Steel

Copyright © by DILAPRO All Rights Reserved | D2.2 – Database for thermal effects on microstructure and mechanical properties of DILAFACT materials

STEM	Scanning Transmission Electron Microscopy
TEM	Transmission Electron Microscopy
UNS	Unified Numbering System
UTS	Ultimate Tensile Strength
WAAM	Wire Arc Additive Manufacturing
XRD	X-Ray Diffraction
YS	Yield Strength

2. Executive Summary

This deliverable presents a database on the effects of process and heat treatments on the microstructure and mechanical properties of materials studied in the DILAFACT project. The study focuses on three materials: austenitic stainless steel 316L, Ni-based superalloy IN625, and Ni-based superalloy IN718. It examines the effect of process parameters, microstructure, and mechanical properties. It is demonstrated that all three materials can be successfully processed using various additive manufacturing (AM) technologies, including Laser Powder Bed Fusion (LPBF), Wire Arc Additive Manufacturing (WAAM), and Directed Energy Deposition (DED), achieving nearly full densification. The LPBF process produces finer microstructures compared to WAAM and DED due to higher cooling rates observed in the LPBF process. The grain interiors commonly exhibit cellular or dendritic morphologies. The finer microstructures associated with LPBF lead to higher tensile strength, but lower tensile ductility compared to the coarser structures produced by WAAM and DED. The AM processed materials exhibit mechanical properties that are comparable to or surpass those of their conventionally manufactured counterparts. In the case of IN718, post-process aging treatments significantly enhance tensile strength due to the precipitation of strengthening γ' and γ" phases, although this also leads to a reduction in ductility. It should be noted that this Deliverable is a resubmission to include more data on IN625 and SS316L for the review meeting, but that it will be further revised and resubmitted after missing data for IN718 will be added and additional thorough analysis of data will be performed.

Copyright © by DILAPRO All Rights Reserved | D2.2 – Database for thermal effects on microstructure and mechanical properties of DILAFACT materials

3. Effect of process parameters and heat treatments on the microstructure and mechanical properties

3.1 Stainless steel 316L

3.1.1. Specifications

Table 1 below presents the chemical composition of the Stainless Steel (SS) 316L according to the standards: [1 - 3]. As is seen, SS 316L composition features maximum carbon levels of 0.03 wt. %. The silicon levels peak at a maximum of 0.75 wt. %. Maximum manganese, phosphorus, nitrogen, and sulfur levels are set at 2 wt. %, 0.045 wt. %, 0.1 wt. % and 0.03 wt. %, respectively. The SS 316L is composed of chromium at 16 wt. % min and 18 wt. % max. Nickel levels are set at 10 wt. % min and 14 wt. % max. The molybdenum content is a minimum level of 2 wt. % and a maximum of 3 wt. %. Enhanced chromium content provides corrosion (oxidation) resistance and improves hydrogen embrittelement resistance. Nickel is an effective austenite stablilizer, as well as helps to reduce cracking and distortion during heat treatment. Manganese increases strength, toughness and hardenability of the material, whereas molybdenum increases resistance to pitting and crevice corrosion, as well as can help to stabilize microstructure at high temperatures [4].

Table 1. Chemical composition (wt. %) of SS 316L according to specifications.

Element	Cr	Ni	Mo	C	Mn	P	S	Si	N	Fe
Min.	16	10	2	-	-	-	-	-	-	-
Max	18	14	3	0.03	2	0.045	0.03	0.75	0.1	bal.

SS 316L maintains a minimum ultimate tensile strength (UTS) of 485 MPa and minimum yield strength (YS) of 120 MPa at 0.2% proof of stress. It has minimum fatigue endurance limit of 256 MPa. It has an elongation of 40 % in 50 mm/min and maximum hardness of 95 kg under the Hardness Rockwell B test. SS 316L reaches a maximum hardness of 217 kg under the Brinell scale test.

Copyright © by DILAPRO All Rights Reserved | D2.2 – Database for thermal effects on microstructure and mechanical properties of DILAFACT materials

Table 2. Mechanical properties of SS 316L for the most widely used flat-rolled products (plate, sheet and coil) according to [1].

UTS [MPa]	YS at 0.2 % proof [MPa]	Elongation (% in 50 mm/min)	Endurance limit [MPa]	Hardness Rockwell (HRB) max	Hardness Brinnel (HB) max
485	170	40	256	95	217

Thanks to its high strength and excellent corrosion resistance, SS 316L is widely used across various engineering sectors [4], including but not limited to equipment for food preparation, pharmaceutical processing, marine applications, medical implants, and chemical transportation. **In the DILAPRO project, SS 316L will be used to manufacture valve brackets and valve wheels via LPBF for oil and gas installations in marine environments (FIELDMADE). It will also be used for the repair of centrifugal impeller blades via DED, restoring them to their original geometry (Prima Additive), for similar applications**, as described in Deliverable 1.1 of the DILAPRO project.

3.1.2. Mechanical properties of SS 316L after additive manufacturing

Mechanical properties of SS 316L after various additive manufacturing processes are summarized in Table 3 below. Most of the published research focuses on using laser powder bed fusion (LPBF), also often referred to as selective laser melting (SLM), technologies for additive manufacturing of SS 316L, typically with layer thicknesses in the range of 20–50 µm. It can be seen that LPBF leads to improved mechanical strength (Table 3) compared to conventional SS 316L alloy (Table 2).

In most cases, the yield strength of LPBF-produced material exceeds 450 MPa (Table 3), which is approximately 2.5 times higher than that of the conventional counterpart (Table 2). Similarly, higher UTS values (above 555 MPa in most cases) are observed in LPBF-manufactured material compared to the conventional one (485 MPa). Meanwhile, elongation-to-failure values vary in the range of 30–60 %, depending on the process parameters, whereas the conventional material shows a minimum of 40 % tensile elongation. It should be noted that tensile elongation can also depend on sample geometry. The fatigue limit of the LPBF-processed materials is in the range of 200 – 425 MPa which can be related to varying quality of the printed material, since fatigue life in the high cycle regime strongly depends on the quality (porosity, presence of microcracks, etc.) of the material.

Wire arc additive manufacturing (WAAM) - processed samples show lower yield strength (220–295 MPa) compared to LPBF samples (Table 3), though still higher than that of the conventional

Copyright © by DILAPRO All Rights Reserved

material (170 MPa). The ultimate tensile strength of WAAM samples (502–560 MPa) is comparable to that of LPBF counterparts and higher than that of the conventional counterpart.

Post heat-treatment of the AM processed SS316L can significantly modify its mechanical properties depending on the heat treatment parameters. In [31], a notable increase in tensile elongation from around 36 % in as-LPBF-fabricated samples to around 65 % in samples treated at 1000 ^{o}C was observed, while YS and UTS exhibited a simultaneous decrease (22 % decrease in samples treated at 1000 ^{o}C than the as-LPBF-fabricated specimen) (Table 3). However, this tensile strength was considerably higher than the wrought counterpart (Table 2, Table 3) [31]. Similar observations were reported for the LPBF processed SS316L alloy in [33]. Heat treatments at 500 oC did not affect mechanical properties of the SLM processed material [32]. It should be noted that heat treatment of the AM processed materials increased manufacturing costs. Therefore, it was out of scope in the DILAPRO project.

Overall, SS 316L produced by LPBF can exhibit an excellent combination of enhanced tensile strength, ductility and fatigue resistance. **The LPBF processed SS 316L in the DILAPRO project showed similar or better level of tensile properties and fatigue resistance when compared to literature data** (Table 3) **and well exceeding the mechanical properties of the conventional counterpart** (Table 2).

Table 3. Mechanical properties of SS 316L after various additive manufacturing processes.

Process parameters	Tensile properties			Fatigue		Source
	YS [MPa]	UTS [MPa]	Elongation to failure [%]	Testing parameters	Fatigue limit σ_{max} [MPa]	
SLM, layer thickness - 30 µm	512	635	32			[5]
LPBF	479	565	41	R=0.1	250	[6]
LPBF	551	620	73.7	R=0.1	207	[7]
SLM, layer thickness - 40 µm	465	555	13.5	-	-	[8]
LPBF, layer thickness - 30 µm	506	638	31	-	-	[9]
SLM - DSM processed; Layer thickness – 30 µm	495	640	57	-	-	[10]
SLM	455	579	50	-	-	[11]
SLM. Horizontal	-	590	21.1	-	-	[12]
Layer thickness – 40 µm; LPBF	423	568	51	-	-	[13]
LPBF, wire-EDM	513	651	53.7	-	-	[14]
LPBF, <111> orientation	710	840.8	58.5	-	-	[15]
Layer thickness - 20-50 µm; LPBF	-	625	56.1	-	-	[16]
Layer thickness – 30 µm; BJP	198	556	66	-	-	[17]
Layer thickness – 30 µm; SLM	511	621	20	-	-	

Copyright © by DILAPRO All Rights Reserved

Layer thickness 30 µm; LPBF	563	709.9	48.3	-	-	[18]
Layer thickness 30 µm; LBM	590	705	44	-	-	[19]
GMA-AM	235	533	48	-	-	[20]
SLM	453	515	7.6	-	-	[21]
SLM	496	717	28	-	-	[22]
SLM	462	565	53.7	-	-	[23]
SLM	511	621	20	-	-	[17]
SLM	430	510	12	-	-	
SLM. 0º	456.8	588.1	-	-1	200	[24]
SLM. 90º	312.6	575.3	-	-1	200	
WAAM. As built. 0º	295.7	502.4	47.1	-	-	[25]
WAAM. As built. 0º	220	560	60	-	-	[26]
SLM. As built	640	760	30	0.1	266	[27]
LPBF	650	750	50	0.1	425	[28]
LPBF. As built	580	710	43	0.1	410	[29]
L-DED. Horizontal. As built	473	665	38	-	-	[30]
L-DED. Horizontal; Heat Treated	378	633	40	-	-	
L-DED. Vertical; As built	387	600	37	-	-	
L-DED. Vertical; Heat Treated	310	567	35	-	-	
LPBF, Layer thickness – 30 µm	500	595	39.2	-	-	[31]
Annealed at 650 ºC, 2 h	430	579	52.4	-	-	
Annealed at 850 ºC, 2 h	365	565	57.5	-	-	
Annealed at 1000 ºC, 2 h	319	539	63.3	-	-	
SLM	482	580	27	-	-	[32]
Annealed at 500 ºC, 2 h	487	602	16	-	-	
Annealed at 500 ºC, 4 h	484	601	17	-	-	
Annealed at 650 ºC, 2 h	435	581	25	-	-	
Annealed at 900 ºC, 1 h	390	576	31	-	-	

LPBF. // BD
LPBF. ⊥ BD
	504
	527
		613
		686
			94
			64
				R=0.1, // BD
				R=0.1, ⊥ BD
					390 MPa
					460 MPa
						DILAPRO

3.1.3 Microstructures of the SS 316L after additive manufacturing

Figure 1 illustrates a complex and heterogeneous microstructure reported in the literature for LPBF-processed SS 316L [34]. The material exhibits nearly full density, with the volume fraction of voids well below 1 %. Melt pools are identifiable (Fig. 1b). The microstructure displays unconventional grain shapes and distributions, along with a nearly random crystallographic

texture (Fig. 1b). Fusion boundaries, as well as dendritic and cellular structures, are evident. EBSD measurements show that LPBF SS 316L contains a high fraction of low-angle grain boundaries (LAGBs), accounting for 41% of the total grain boundaries (GB) (Fig. 1g). The kernel average misorientation (KAM) map indicates the presence of geometrically necessary dislocations (GNDs), with KAM values in the range of 1–1.5°, which correlate with the LAGBs (Fig. 1h). A solidification cellular structure is observed, with an average cell size below 1 µm. Energy Dispersive Spectroscopy (EDS) mapping reveals segregation of Cr and Mo along the walls of the solidification cellular structures and LAGBs (Fig. 1i). These cellular walls are decorated with a high density of GNDs (Fig. 1d), as confirmed by the corresponding High-Angle Annular Dark Field (HAADF) – Transmission Electron Microscopy (TEM) image.

The microstructure of WAAM-processed SS 316L differs significantly from that observed in the LPBF-produced samples. WAAM printing results in dispersed, micrometer-sized inclusions and voids, with most having areas between 0.15 and 0.5 µm² (Fig. 2a, b). Typical columnar dendritic grain structures are observed in cross-sectional views (Fig. 2c), and grains are coarser compared to the LPBF microstructures. The austenitic matrix contains a small fraction of *δ*-ferrite and a very limited amount of brittle *σ*-phase, visible as green and blue lamellae in Fig. 2d.

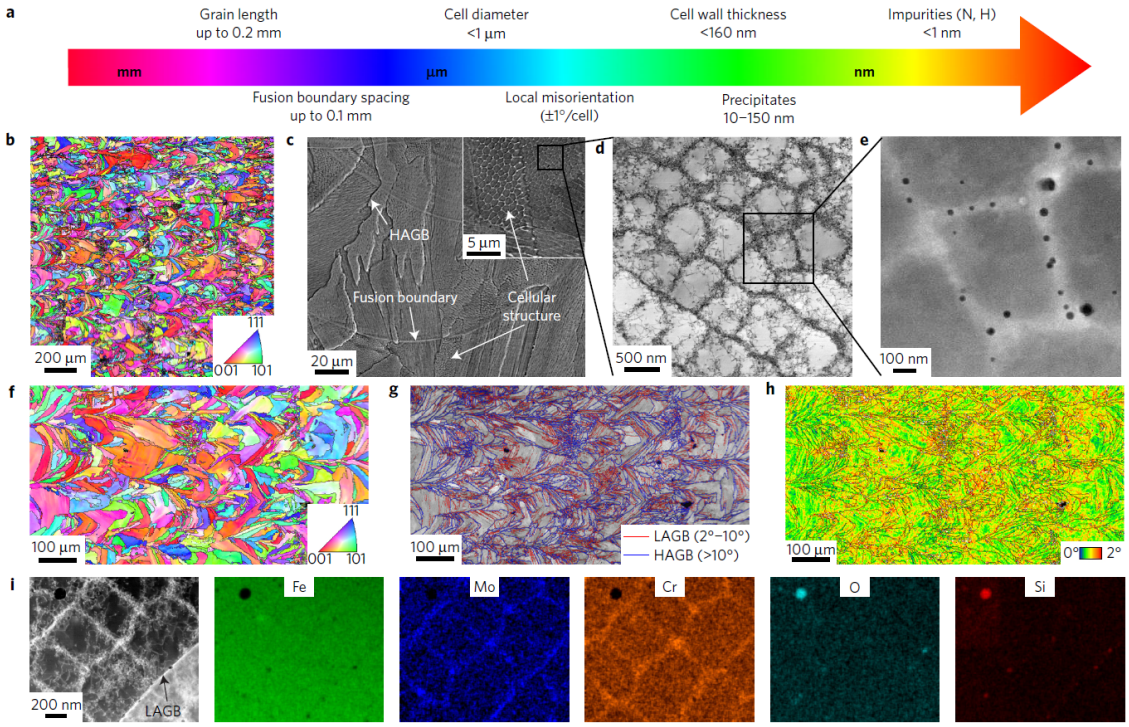


Figure 1 (reproduced from [34]). *Typical microstructure of a LPBF produced SS 316L:* ***a)*** *A schematic of various length scales uncovered in LPBF SS 316L SS;* ***b****) A cross-sectional EBSD inverse-pole figure (IPF) map of the as-built SS 316L showing grain orientations. The IPF map was acquired with a 2 µm step size. The build direction is horizontal.* ***c****, A cross-sectional SEM image, revealing fusion boundaries, high-angle grain boundaries (HAGBs), and solidification cellular structures. The*

Copyright © by DILAPRO All Rights Reserved | D2.2 – Database for thermal effects on microstructure and mechanical properties of DILAFACT materials

inset shows the cellular structure at a higher magnification. The build direction in this image is vertical; ***d****) A bright-field transmission electron microscopy (TEM) image of solidification cells;* ***e****) A high-angle annular dark-field (HAADF) scanning TEM (STEM) image of the solidification cells shown in* ***d****. The nanoparticles segregated to the cell walls were identified as transition-metal-rich silicates formed during LPBF processing;* ***f****) EBSD IPF map acquired with a 1-µm step size;* ***g****) EBSD image quality (IQ) map with HAGBs and low-angle grain boundaries (LAGBs) superimposed. As indicated in the legend, HAGBs (>10°) are coloured blue and LAGBs (2–10°) are coloured red. The fraction of HAGBs and LAGBs are 59 % and 41 %, respectively;* ***h****) A map of the kernel average misorientation (KAM), measured in degrees, to illustrate the local misorientation across individual grain. It is evident that all of the grains have local misorientations on the order of 0.5–1°;* ***i****) A HAADF STEM (Z contrast) image showing segregation of Mo and Cr to the solidification cellular walls and a LAGB, with corresponding Fe, Mo, and Cr energy-dispersive spectroscopy (EDS) maps that confirm this segregation. The EDS map also verifies that particles are mostly rich with Si, O, and Mn.*

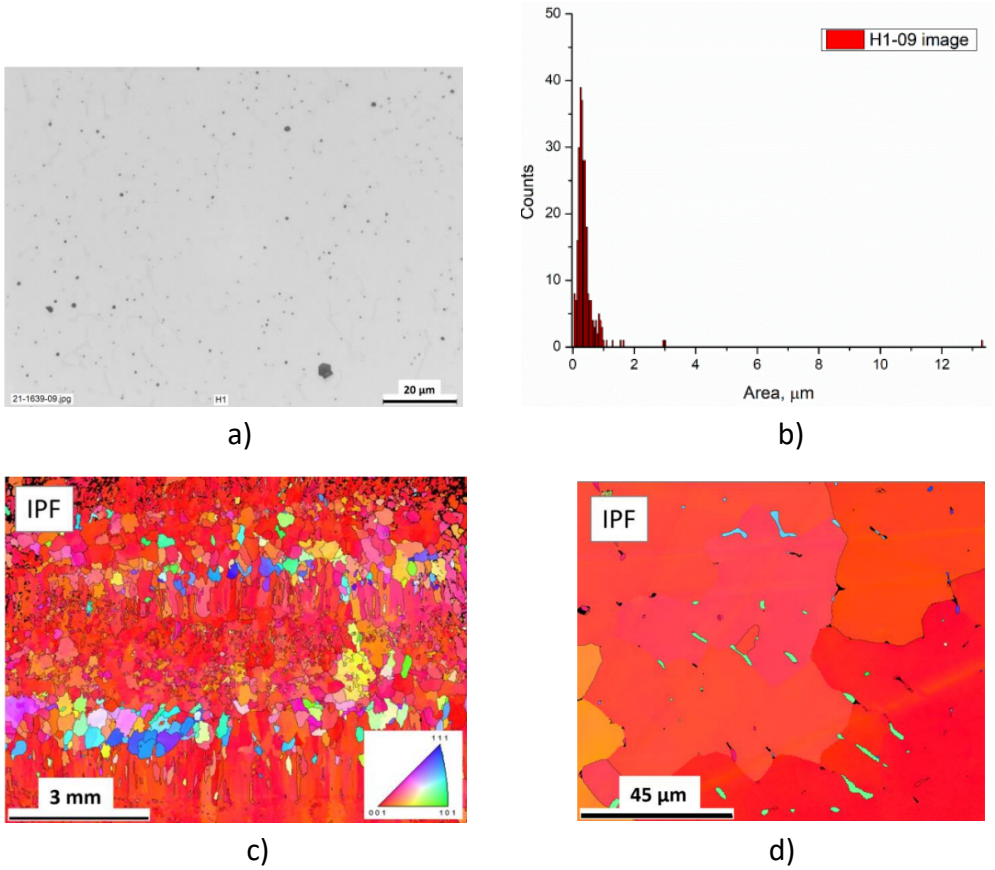


Figure 2 (reproduced from [34]). *Microstructure of the WAAM manufactured SS 316L (building direction - vertical): a) Cross-section montage and high-magnification image of H1 specimen; b) typical inclusions/voids sizes and distributions of specimens removed along height; c) IPF map along height (low magnification); d) IPF map along height (high magnification).*

Copyright © by DILAPRO All Rights Reserved | D2.2 – Database for thermal effects on microstructure and mechanical properties of DILAFACT materials

Inverse pole figure (IPF) maps reveal variations in grain shapes, orientations, and sizes, primarily along the vertical (building) direction. These variations are attributed to the shifting direction of the welding torch during the WAAM process. The resulting grain structures are characteristic of the columnar dendritic formations typically produced during solidification in WAAM. The microstructure of the WAAM material is inhomogeneous (Fig. 2 c, d), but generally much coarser compared to that of the LPBF counterpart (Fig. 1f) due to lower cooling rates in WAAM process. For instance, cooling rates between 1000 ^{o}C/s and above 5000 ^{o}C /s were experimentally measured in [35] depending on the WAAM process parameters. Much higher cooling rates of ≥ 15.000 ^{o}C/s were measured during LPBF process, although this cooling rate can drop down to ~ 5.000 ^{o}C/s when the base plate is additionally pre-heated [36]. This results in lower YS and UTS and higher ductility shown by WAAM samples compared to LPBF samples (Table 3).

It should be noted that post heat-treatment of the AM processed SS316L can significantly modify the microstructure of the material. For example, a complete disappearance of melt pool boundaries occurred above 650 ^{o}C, and the cellular structure disappeared for the samples heat treated at 850 ^{o}C and 1000 ^{o}C indicating the annihilation of dislocations, which resulted in reduction of material's strength [31] (Table 3).

Figure 3 illustrates the complex microstructure with unconventional grain shapes and distributions for LPBF SS 316L manufactured by DTI in the DILAPRO project. The as-printed material is nearly fully dense and fully austenitic. There is no preferred crystallographic orientation (e.g. it presents a random crystallographic texture, Fig. 3c). The enhanced local KAM values are observed along LAGBs and do not exceed 1.3^{o} (Fig. 3d). A few microcracks were observed in the large, printed sample, and their length does not exceed 20 µm (Fig. 3b). The microcracks did not show any preferred orientation with respect to the building direction. The EDS analysis did not reveal the presence of any noticeable segregations of alloying elements (Fig. 3e) even along the microcracks or at their tips.

Copyright © by DILAPRO All Rights Reserved

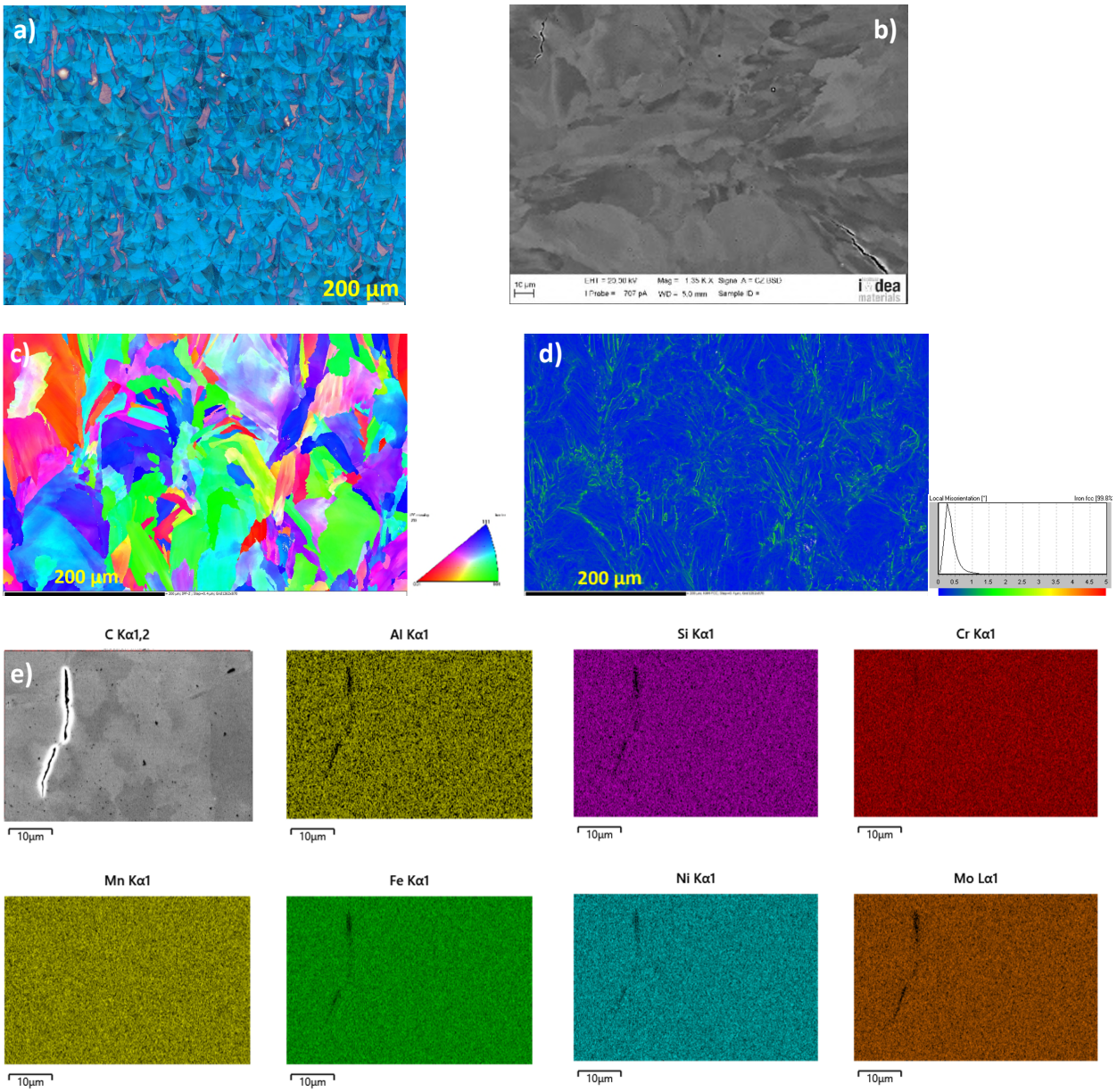


Figure 3 (DILAPRO Data). *Microstructure of the LPBF manufactured SS 316L (building direction - vertical): a) general view of microstructure in optical microscope; b) SEM image taken using backscatter detector (BSD); c) IPF map; d) corresponding KAM map; e) secondary electron (SE) image showing microcracks and corresponding elemental maps.*

Copyright © by DILAPRO All Rights Reserved | D2.2 – Database for thermal effects on microstructure and mechanical properties of DILAFACT materials

3.2 Inconel 718

3.2.1. Specifications

IN718 is a nickel-chromium-molybdenum alloy designed to resist a wide range of severely corrosive environments, pitting and crevice corrosion. Table 4 below presents the chemical composition of the nickel-based IN718 according to the standards [37-39]. One of the distinguishing features of IN718's composition is the addition of niobium (4.75 wt. % min) to permit age hardening which allows annealing and welding without spontaneous hardening during heating and cooling. The addition of niobium acts with the molybdenum (2.8 wt. % min) to stiffen the alloy's matrix and provide high strength without a strengthening heat treatment. It is also age hardened through the addition of aluminum (0.2 wt. % min) and titanium (0.65 wt. % min).

Table 4. Chemical composition (wt. %) of IN718 according to specifications.

	Cr	Mo	Nb	Ni	Ti	Al	Co	Si	Mn	C
Min.	17	2.8	4.75	50	0.65	0.2	-	-	-	-
Max.	21	3.3	5.5	55	1.15	0.8	1	0.35	0.35	0.08

	Ta	P	S	Cu	B	Pb	Se	Bi	Fe
Min.	-	-	-	-	-	-	-	-	-
Max.	0.05	0.015	0.015	0.3	0.006	0.0005	0.002	0.00003	bal.

IN718 maintains a minimum UTS of 1240 MPa and minimum YS of 1035 MPa at 0.2% proof of stress (Table 5). It has an elongation of 12 % in 50 mm/min and maximum hardness of 331 kg under the Brinell scale test. IN718 also displays exceptionally high YS and UTS at high temperatures. This superalloy alloy is used from cryogenic temperatures up to long term service at high temperatures (up to 650 ^{o}C). For most applications, IN718 is specified as precipitation hardened (aged). The aging treatment for IN718 typically involves a two-step process to enhance its strength and other mechanical properties. It consists of a solution treatment followed by one or two aging stages. The solution treatment involves heating the material to a high temperature (e.g. 1100 °C) to dissolve certain phases (such as Laves phase). The aging process then involves holding the material at lower temperatures (e.g. 620 – 950 °C) to precipitate desired phases like gamma prime (γ') and gamma double prime (γ''), which significantly improve strength. The exceptional strength of the material also remains effective even at extremely low (cryogenic) temperatures. This makes it an ideal choice for components that must perform reliably under cryogenic conditions, ensuring they can withstand significant stress without deforming.

Copyright © by DILAPRO All Rights Reserved | D2.2 – Database for thermal effects on microstructure and mechanical properties of DILAFACT materials

Table 5. Mechanical properties of IN718 at room temperature for plate according to [40, 41].

	UTS [MPa] min	**YS at 0.2 % proof [MPa] min**	**Elongation (% in 50 mm/min)**	**Endurance limit [MPa]**	**Hardness Brinnel (HB) max**
Hot rolled and annealed at 955 °C / 1 h	810	380	53	-	-
Solution treated + aged	1240	1035	12	256	331

The unique properties of IN718 enable its widespread use across various engineering sectors [42], including aero-engine and gas turbine components, liquid-fuel rocket motor parts, and nuclear reactors. **In the DILAPRO project, a fuel valve will be manufactured from IN718 via LPBF by DCU for use in the space industry.** This component will support a critical system in a launch vehicle's cryogenic rocket engine, as detailed in Deliverable 1.1 of the DILAPRO project.

3.2.2. Mechanical properties of IN718 after additive manufacturing

Mechanical properties of IN718 after various additive manufacturing processes and heat treatments are summarized in Table 6 below. As it is seen, the YS and UTS strength values of the as-printed IN718 after LPBF (640 - 750 MPa and 940 - 1040 MPa, respectively) are higher and tensile ductility (29 - 35 %) is lower compared to the hot rolled and annealed counterpart (Table 5). The further solution treatment of the LPBF sample followed by aging treatment significantly improves YS and UTS (1092 MPa and 1323 MPa, respectively) which are higher compared to the solution-treated and aged conventional counterpart (1035 MPa and 1240 MPa), whereas ductility is also slightly better for the LPBF processed, solution-treated and aged counterpart (14 % vs 12 % for the conventional counterpart). In [43], it was shown that 1100 °C is the optimum temperature for solution treatment of IN718 resulting in best tensile properties. Similar level of tensile mechanical properties is demonstrated by DLD solution treated and aged IN718. LPBF-processed IN718 shows modest level of fatigue limit (150-260 MPa) probably related to high density of the defects present in the materials.

The WAAM processed material follows the same trend. In the as-deposited condition, it shows low YS and UTS values (473 MPa and 841 MPa, respectively), which further increase after solution treatment and aging (836 MPa and 1158 MPa). The WAAM material retains high tensile ductility after aging treatment (16.4 %). DLD processed material shows somewhat higher level of strength. After solution treatment and aging, the reported values of YS are above 1000 MPa and UTS values are above 1220 MPa while tensile elongation is slightly lower being in the range of 9.8 – 16 %. Overall, IN718 produced by LPBF or DLD can exhibit an excellent combination of enhanced tensile

Copyright © by DILAPRO All Rights Reserved | D2.2 – Database for thermal effects on microstructure and mechanical properties of DILAFACT materials

strength and ductility. Results from the mechanical characterization of IN718 manufactured in the DILAPRO project will be added to the revised document after completing characterization of these samples.

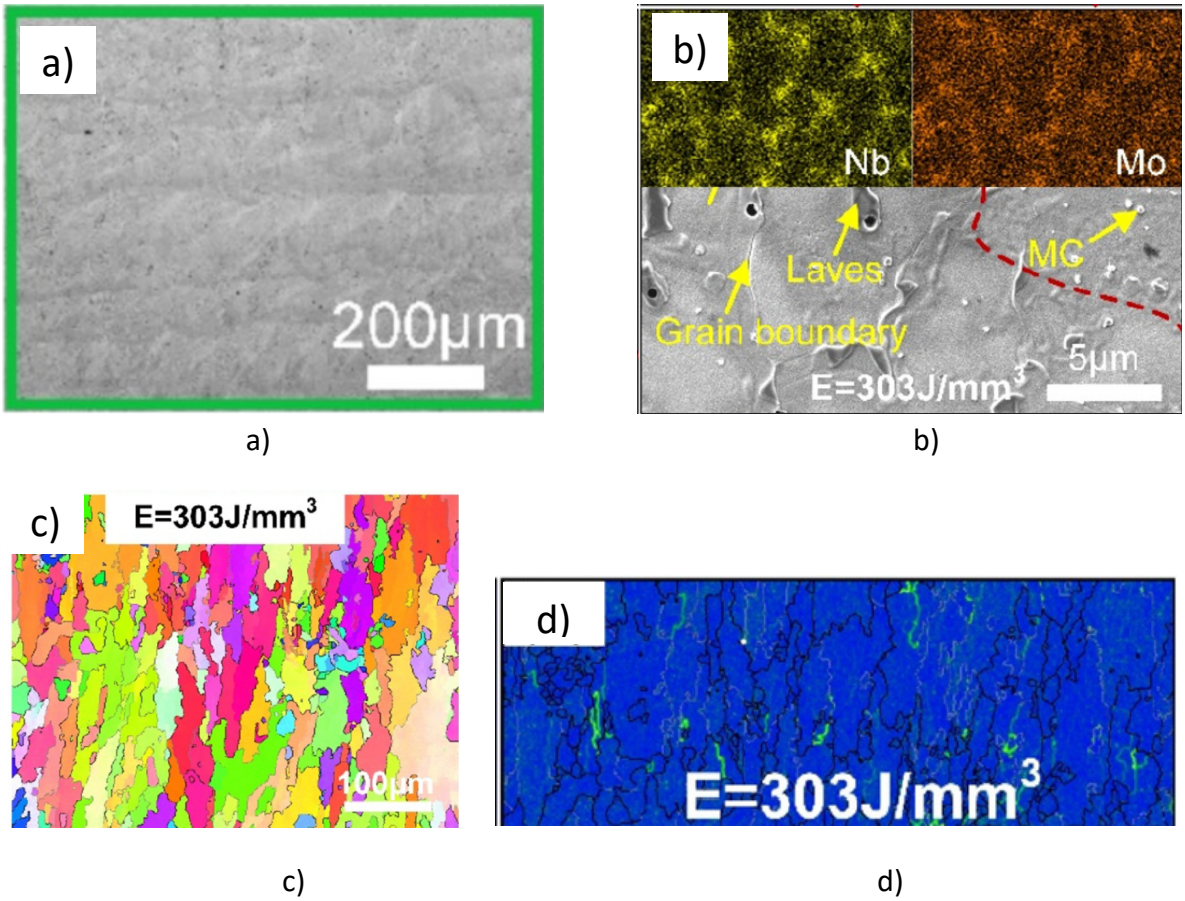
Table 6. Mechanical properties of IN718 after various additive manufacturing processes.

Process parameters	**Tensile properties**			**Fatigue**		**Source**
	YS [MPa]	UTS [MPa]	Elongation to failure [%]	Testing parameters	Fatigue limit [MPa]	
SLM; As built samples	640	940	35	R = -1	150	[44]
LPBF; Printed in X/Y direction, as-printed condition	750	1040	29	R = 0	260	[45]
DLD, Solution + aging	1098	1321	9.8			[46]
SLM; Heat Treated (Homogenisation + Solution + Aging)	1092	1323	14			[47]
SLM; Heat treated (Solution + Aging)	1126	1336	14			
WAAM; As deposited	473	841	26.3			[48]
WAAM; Heat Treated(Solution + Aging)	836	1158	16.4			
Layer thickness – 30 µm; SLM; As-Built	680	970	31.6			[49]
Layer thickness – 30 µm; SLM; Surface machined	733	1018	25.9			
Layer thickness – 30 µm; SLM; Heat Treated	963	1195	15.8			
Layer thickness – 30 µm; SLM - As fabricated; Longitudinal	711	1110	24.5			[50]
Layer thickness – 30 µm; SLM - As Fabricated; Transverse	858	1167	21.5			
SLM; As-built	572	904	19			[51]
SLM; Heat Treated (Solution + Aging)	1240	1400	-			
EBM; As-built (parallel orientation)	793	809	1			[52]
EBM; As-built (perpendicular orientation)	815	879	8.5			
SLM	1400	1600	16			[53]
LPBF; Heat Treated	1180	1380	16			[54]
DLD; Heat Treatment (Solution Anneal + Aging)	1007	1221	16			[55]
DLD; Heat Treatment (Homogenization + Solution Anneal + Aging)	1034	1276	12			
DLD; Heat Treatment (Solution Anneal + Aging)	1257	1436	-			
Layer thickness – 160 µm; SLM - As Fabricated, Longitudinal	572	904	19			[43]
Layer thickness – 160 µm; SLM, Heat treated (Solution + Aging), Longitudinal	1074	1320	19			

Copyright © by DILAPRO All Rights Reserved | D2.2 – Database for thermal effects on microstructure and mechanical properties of DILAFACT materials

3.2.3 Microstructures of the IN718 after additive manufacturing

There is a significant effect of AM parameters on the quality and microstructure of the printed IN718 alloy. Optimum processing parameters were identified for the IN718 in [56]. In the 18 – 1000 J/mm^3 thermal input range, stable processing windows resulting in nearly dense materials were observed at 48, 89, 148, 303 and 623 J/mm^3 (Fig. 4). In high power density forming, the formation of the Laves phase in the melt pool is inhibited, while the precipitation of MC compounds is significant due to the rapidly changing thermal gradient. There is a segregation of Nb and Mo between layers and at cell boundaries (Fig. 4b). Three distinct grain structure features can be noted for this material (Fig. 4c, d): (1) epitaxial growth with columnar grains, (2) chaotic grains associated with the melt pool, with a higher mean GND density of 1.58 × 10^{14}/m^2, and (3) orderly grains, independent of the melt pool morphology, with a significantly lower GND density. No significant crystallographic texture is observed (Fig. 4c).

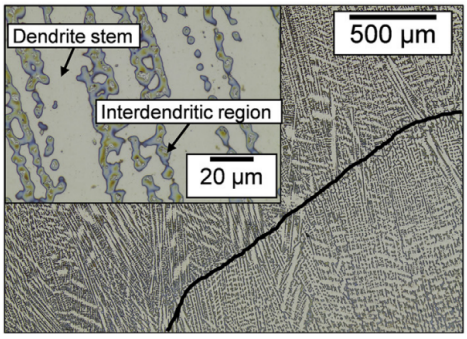


a) b) c) d)

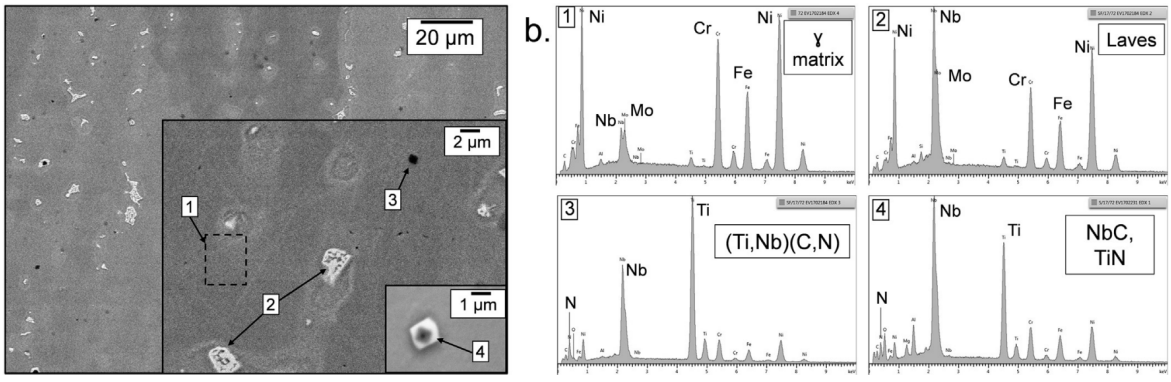
Figure 4 (reproduced from [56])*. Microstructure of the LPBF manufactured IN718 [56] with the power density of 303 J/mm^3 (BD is vertical): a) optical microscopy image; b) SEM images and EDS elemental maps; c) IPF map; d) KAM map.*

Copyright © by DILAPRO All Rights Reserved | D2.2 – Database for thermal effects on microstructure and mechanical properties of DILAFACT materials

The microstructure of the as-deposited WAAM IN718 is much coarser compared to that of the LPBF samples (Fig. 5) [57]. The macrograph insert (Fig. 5a) also shows epitaxial dendrite growth from the substrate plate generally in line with the BD, indicating that the thermal gradient is the highest in this direction. Some dendrites have grown across interlayer boundaries (marked by black line) and can be several millimetres long. The curvature of the interlayer boundaries can be related to the spreading of the molten pool towards the edge during deposition. Laves phase, along with Ti- and Nb-rich inclusions, are observed in the as-deposited microstructure (Fig. 5b). The contrast of the SEM BSE images (Fig. 5a), which is contributed by topography and elemental differences [57], show particle morphology and elemental contrast in the microstructure. The main elements in the γ-matrix, which is represented by Area 1 (marked by a dashed rectangular on SEM image in Fig. 5b), are Ni, Cr and Fe, as shown by their large peaks in the corresponding EDS spectrum in Fig. 5b. Smaller peaks were observed for Nb and Mo. Grains in the as-deposited sample are columnar and elongated along the BD (Fig. 5c). The grains are coarse with length up to several mm as shown in the EBSD maps in Fig. 5c. Most of the grains have ⟨100⟩ direction well-aligned with the BD. Modified homogenisation treatment (HA) at 1186 ^{o}C for 40 min followed by air cooling and a standard double aging treatment (720 ^{o}C for 8 h, furnace cool, and 620 ^{o}C for 8 h, air cool) applied to the material resulted in coarser grain structure, full dissolution of Laves phases in the microstructure and randomization of the crystallographic texture (Fig. 5c,d). Significantly coarser grain structure of the WAAM IN718 results in its lower tensile strength compared to the LPBF samples.



a)



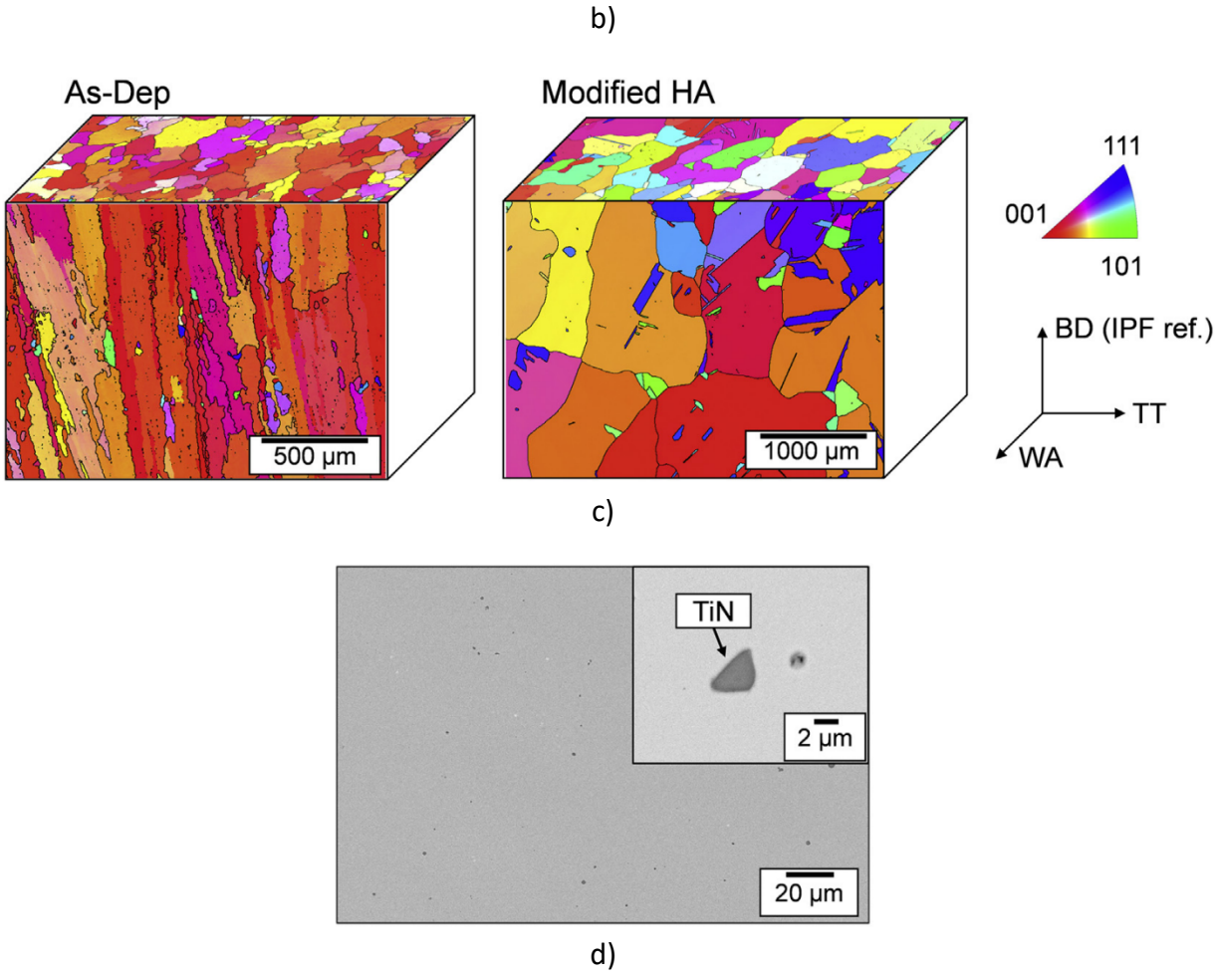


Figure 5 (reproduced from [57])*. Microstructure of the WAAM manufactured IN718 (BD is vertical): a) optical microscopy image of the as-deposited microstructure; b) backscatter electron image and corresponding EDS spectra of the as-deposited microstructure, c) IPF maps of the as-deposited material and heat treated material; d) backscatter electron image of the heat treated material.*

3.3 Inconel 625

3.3.1. Specifications

Inconel 625 (IN625) is a wrought nickel-based superalloy strengthened mainly by the additions of chromium (20 wt. % min), molybdenum (8 wt. % min), niobium + cobalt (3.15 wt. % min) and carbon (0.1 wt. % max), e.g. predominantly solid solution hardened alloy (Table 7). Developed for service at temperatures below 700 °C, this alloy combines the high strength of the age-hardening

Copyright © by DILAPRO All Rights Reserved | D2.2 – Database for thermal effects on microstructure and mechanical properties of DILAFACT materials

nickel-based alloys with excellent fabrication characteristics (Table 8), though its tensile strength is lower compared to that of the precipitation hardened IN718 (Table 5). The high alloy content of IN625 enables it to withstand a wide variety of severe corrosive environments. In mild environments such as the atmosphere, fresh and sea water, neutral salts, and alkaline media there is almost no attack.

Table 7. Chemical composition (wt. %) of IN625 according to specifications [58-62].

	Cr	Mo	Nb/Co	Ni	Ti	Al	Co	Si	Mn	C
Min.	20	8	3.15	58	-	-	0	-	-	-
Max	23	10	4.15	-	0.40	0.40	1.0	0.50	0.50	0.10

	Ta	P	S	Cu	Fe
Min.	-	-	-	-	-
Max	0.05	0.015	0.015	0.50	5.00

IN625 maintains a minimum UTS of 880 MPa and minimum YS of 460 MPa at 0.2 % proof of stress (Table 8). It has an elongation of 50 % in 50 mm/min and maximum hardness of 190 kg under the Brinell scale test. It is characterized by an excellent endurance limit of 621 MPa at room temperature. For service at 650 ^{o}C and below, hot-finished, cold-finished, and annealed conditions (depending on requirements involved) are recommended. For service above 650 ^{o}C, either annealed or solution-treated material provides the best service. The solution-treated condition is recommended for components that require optimum resistance to creep or rupture. Fine-grained (annealed) material may be advantageous at temperatures up to 815 ^{o}C with respect to fatigue strength, hardness, and tensile strength.

Table 8. Mechanical properties of annealed IN625 at room temperature for plate according to specifications [58-59].

UTS [MPa] min	YS at 0.2 % proof [MPa] min	Elongation (% in 50 mm/min)	Endurance limit [MPa]	Hardness Brinnel (HB) max
880	460	50	621	190

Thanks to its high strength and good corrosion resistance, IN625 is widely used in various critical applications [63, 64], such as spacecrafts and submarines, oil and gas, chemical processing industries. **In the DILAPRO project, a spring shoe will be manufactured from IN625 via LPBF by FIELDMADE for automotive applications.** This spring shoe is a complex bracket component designed to be part of the dampening system to mitigate the risk of damage during transport.

Copyright © by DILAPRO All Rights Reserved | D2.2 – Database for thermal effects on microstructure and mechanical properties of DILAFACT materials

3.3.2. Mechanical properties of IN625 after additive manufacturing

The mechanical properties of IN625 after various additive manufacturing processes and heat treatments are summarized in Table 9 below. As shown, in most cases, the as-printed LPBF material exhibits high yield strength (YS) (well above 600 MPa) and ultimate tensile strength (UTS) (well above 900 MPa), exceeding those of the conventional counterpart (Table 8). The tensile ductility of LPBF IN625 is comparable to that of the conventional material (around 50 %). Annealing (stress-relieving) of the LPBF samples results in higher tensile strength and slightly reduced ductility compared to the as-built condition. These variations in mechanical properties can be attributed to the formation of nanometric γ'' phases.

IN625 processed by WAAM and DED shows lower YS (above 350 MPa) and UTS (above 660 MPa), but significantly higher tensile ductility (above 70 %) compared to the LPBF samples. This is likely due to the much coarser microstructure observed in WAAM and DED materials (see Section 3.3.3 below). Other AM processes, such as LRM or LENS, also lead to lower YS and UTS compared to the LPBF processes. The LC processed IN625 shows modest fatigue limit of 160-272 MPa which can be related to the defects present in the printed material. However, the LPBF-processed IN625 manufactured by DTI in the DILAPRO project shows an excellent fatigue limit of ≥520 MPa indicating its high quality.

The effect of post heat treatments on mechanical properties of the LPBF samples was studied in [63]. The stress-relieved samples at 600 ^{o}C did not significantly affect tensile properties with respect to the as-built condition, whereas stress relieving at 800 ^{o}C and 870 ^{o}C resulted in reduction of tensile strength and improvement of tensile ductility (Table 9). The solution annealed samples at 1150 ^{o}C resulted in the highest ductility and the lowest tensile strength among the tested conditions due to recrystallization of microstructure (Table 9).

Table 9. Mechanical properties of IN625 after various additive manufacturing processes.

Process parameters	**Tensile properties**			**Fatigue**		**Source**
	YS [MPa]	UTS [MPa]	Elongation to failure [%]	Testing parameters	Fatigue limit [MPa]	
LC (low-energy). Stress relieved	485	744	43	R = 0	272	[64], [65]
LC (high-energy). Stress relieved	430	697	55	R = -1	160	[65]
Layer thickness – 50 µm; SLM. Horizontal	800	1030	8-10			[8]
Layer thickness -50 µm; SLM. Vertical	720	1070	8-10			
LPBF; As-built	667	939	39			[66]

Copyright © by DILAPRO All Rights Reserved | D2.2 – Database for thermal effects on microstructure and mechanical properties of DILAFACT materials

LPBF; Heat Treated	363	853	62			
DED; As-built	433	779	56			
DED; Heat Treated	360	768	73			
WAAM ; As-deposited in X direction	347	669	82			[67]
SLM; printed in XY direction	859	1242	26.8			[68]
SLM; printed in XZ direction	709	1103	30.0			
LENS; printed in XY direction	598	882	29.9			
LENS; printed in XZ direction	492	835	43,45			
LPBF; As-built	618	891	41			[69]
LPBF; Annealed at 600 °C	775	1033	31			
LPBF; Annealed at 800 °C	807	1057	29			
LPBF; Annealed at 870 °C	715	1017	35			
LPBF; Annealed at 1150 C	430	881	53			
Layer thickness - 100 µm; LPBF	748	1078	9			[70]
LPBF; Layer thickness - 100 µm	687	968	11.5			
LRM	572	920	48			[71]
LRM	568	925	46			
LPBF; 650 °C	660	953	27.2			[72]
LPBF; As-built	743	1043	31.4			[73]
LPBF; Annealed	386	910	54.4			
LPBF (multi-laser); As-built	585	864	58.6			[74]
LPBF (multi-laser); Heat treatment	507	827	69.3			
LPBF; As-built	641.5	878.5	30			[75]

LPBF. // BD
LPBF. ⊥ BD
	364
	702
		885
		1002
			72
			49
				R=0.1, // BD
				R=0.1, ⊥ BD
					520
					540
						DILAPRO

3.3.3 Microstructures of the IN625 after additive manufacturing

The microstructure formed in IN625 after the LPBF process is illustrated in Fig. 6 below. The melt pool structure is clearly visible (marked by arrow on Fig. 6a) [76], [77]. SEM and XRD analyses did not reveal the presence of any secondary phases. However, EDS characterization indicated microsegregation of Nb and Mo along dendrite and cell boundaries (Fig. 6b). The EBSD analysis revealed a complex grain structure without any preferred crystallographic texture (Fig. 6c).

Copyright © by DILAPRO All Rights Reserved

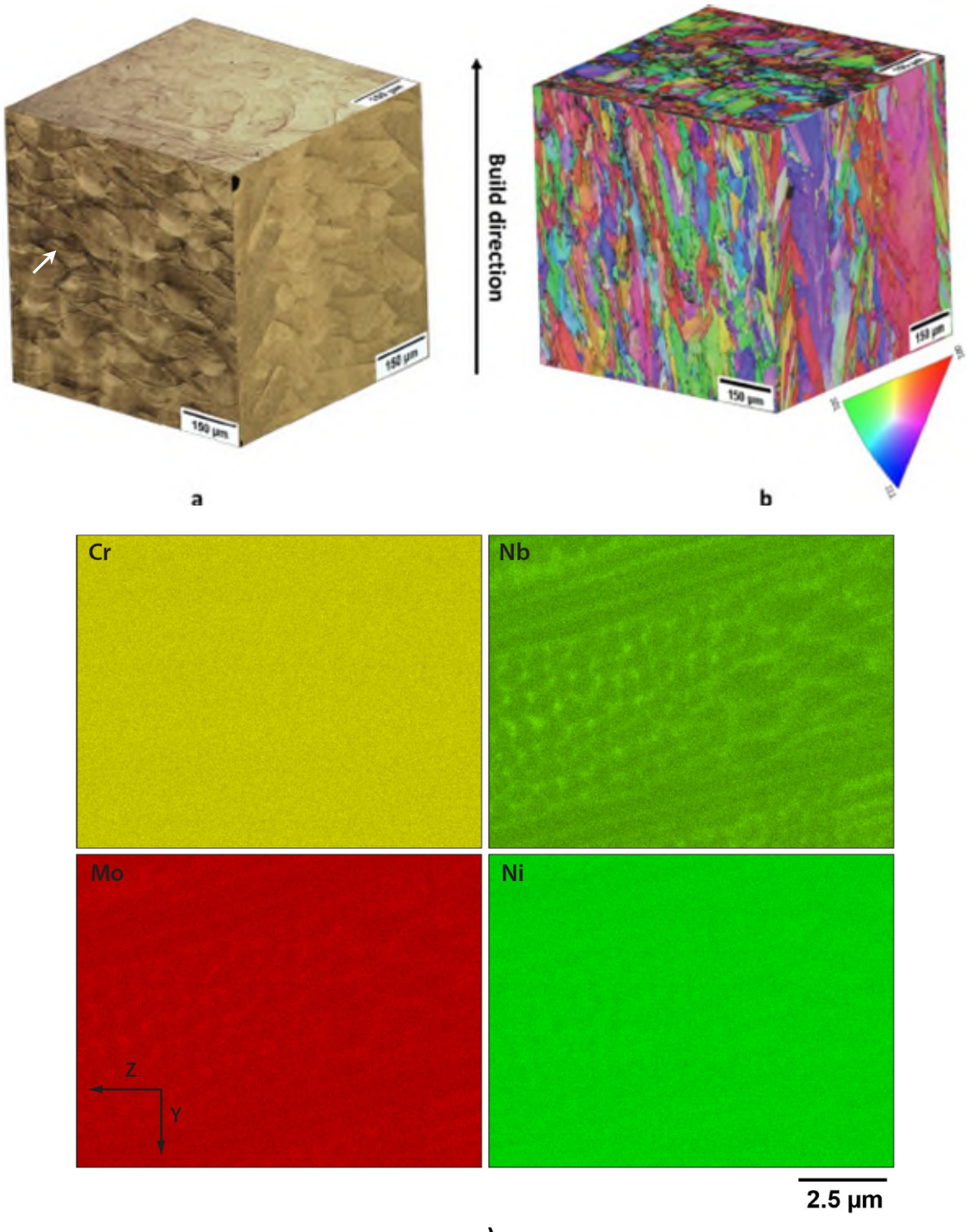
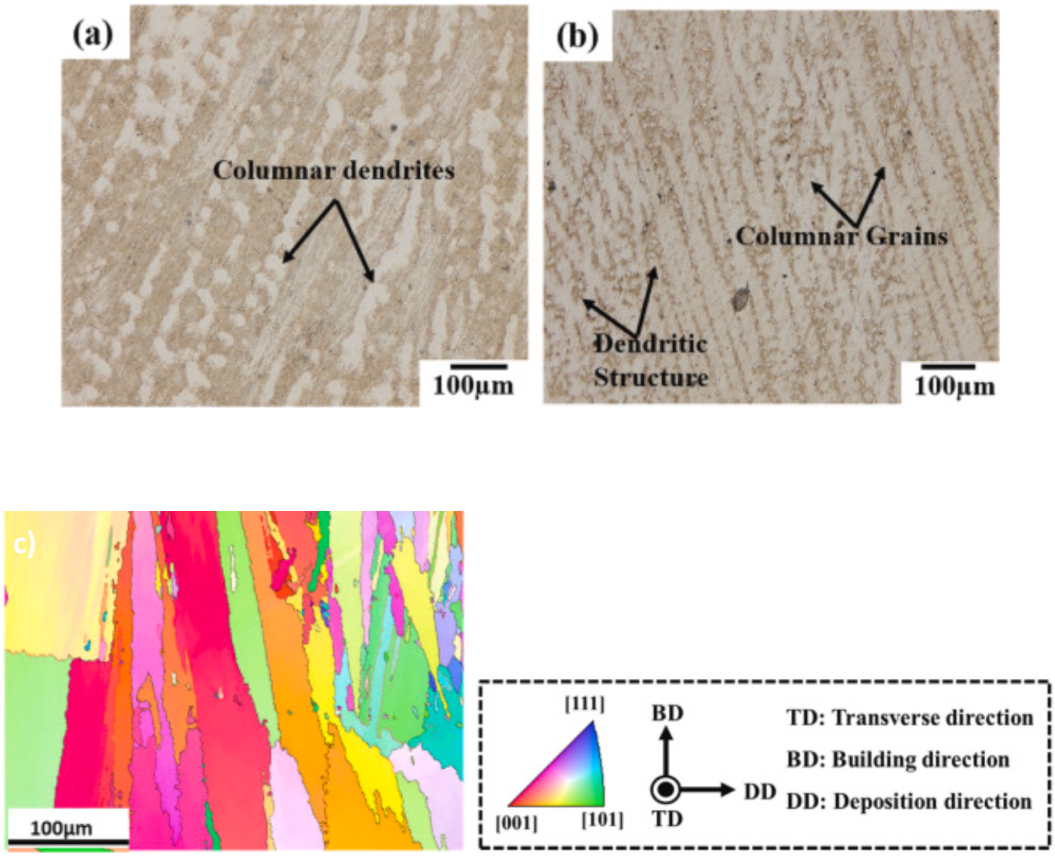


***Figure 6 (reproduced from [76])**. Microstructure of the LPBF processed IN625 (Z corresponds to BD): a) optical microscopy image of the as-printed microstructure (melt pools are visible); b) IPF maps of the as-printed material; c) EDS maps of the as-printed microstructure.*

Copyright © by DILAPRO All Rights Reserved | D2.2 – Database for thermal effects on microstructure and mechanical properties of DILAFACT materials

The microstructure of the WAAM-processed IN625 alloy at the mid-height of the wall is presented in Figure 7 [77]. The microstructure consists of columnar dendrites that span multiple layers and are nearly parallel to the building direction, along with a cellular structure. Grain growth is primarily dictated by the direction of heat flux. The columnar grains, aligned with the build direction, show no strong crystallographic texture (Fig. 7c). Most of the grain boundaries are HAGBs. The KAM map shows relatively low local misorientation values, not exceeding 1.5°, primarily observed at LAGBs, while the grain interiors exhibit nearly zero local misorientation.

It should be noted that the grain structure may vary along the build direction. Overall, the WAAM-processed material is characterized by coarser columnar grains compared to the LPBF samples, which contribute to its lower strength and higher tensile ductility. Overall, IN625 showing excellent combination of enhanced strength and tensile ductility can be manufactured via LPBF processes.



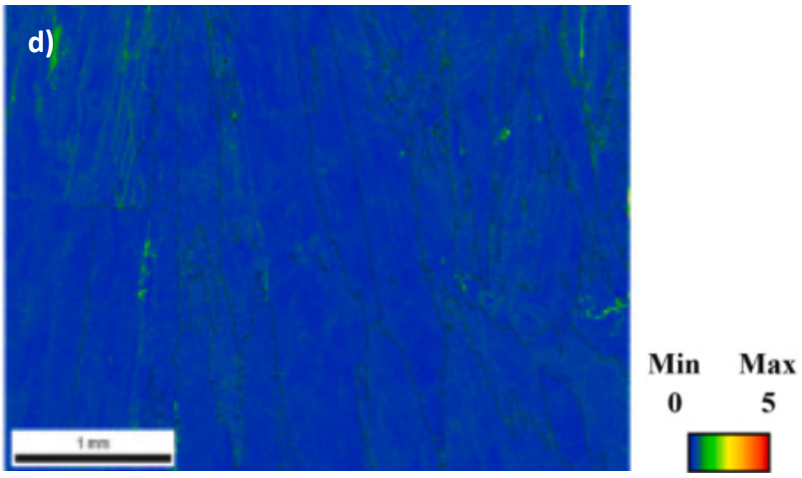
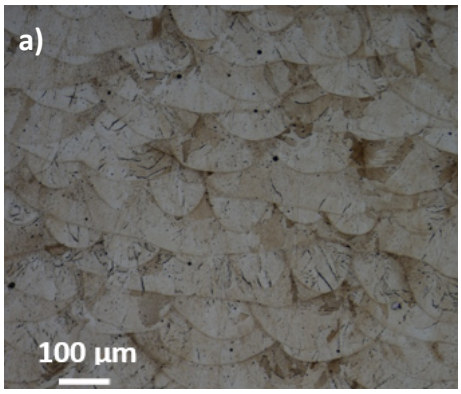


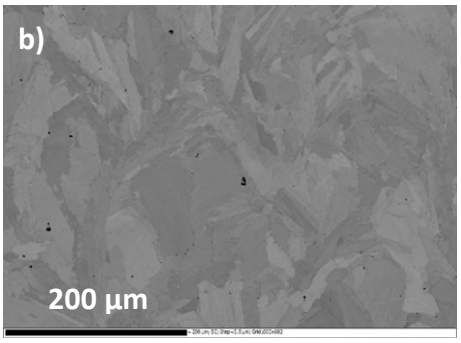
Figure 7 (reproduced from [77]). *Microstructure of the LPBF processed IN625 in the middle region of wall (BD is vertical): a, b) optical microscopy images of the as-printed microstructure; c) EBSD IPF map of the as-printed microstructure, d) corresponding KAM map of the as-printed microstructure.*

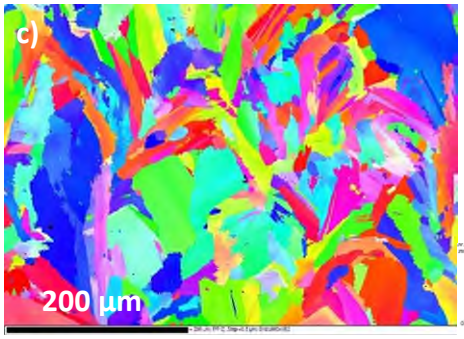
The effect if post heat treatments on the microstructure of LPBF IN625 was analyzed in [69]. The stress-relieving at 600 °C did not affect the microstructure and dislocation structure. However, stress relieving at 800 °C resulted in the formation of Cr-rich M23C6 carbides and at 870 °C led to generation of δ phase. Fully recrystallized microstructure was observed after annealing at 1150 °C.

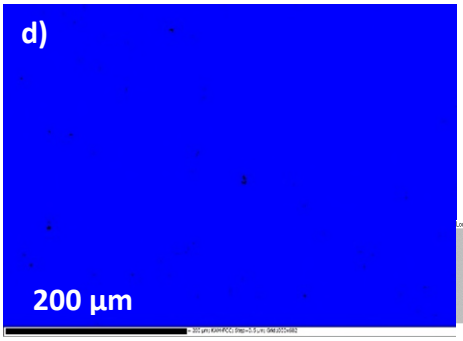
Figure 9 illustrates the microstructure of the LPBF IN625 manufactured by DTI in the DILAPRO project. It is fully dense, and no microcracks have been observed. The EBSD analysis revealed the complex microstructure with unconventional grain shapes and distributions without any defined crystallographic texture (Fig. 9c). The KAM map shows enhanced misorientation angles (up to 1.7°) along LAGBs. The microstructure is characterized by fine cellular/dendritic structure (Fig. 9e). The EDS analysis carried out at different magnifications did not reveal any significant microsegregations of alloying elements.

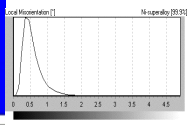
Copyright © by DILAPRO All Rights Reserved



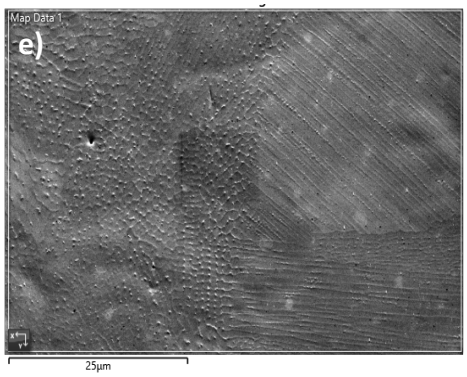


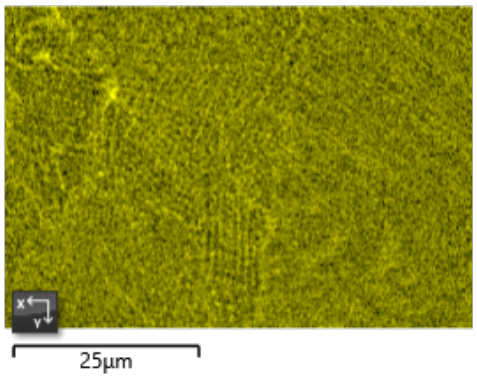






Nb Wt%





Copyright © by DILAPRO All Rights Reserved | D2.2 – Database for thermal effects on microstructure and mechanical properties of DILAFACT materials

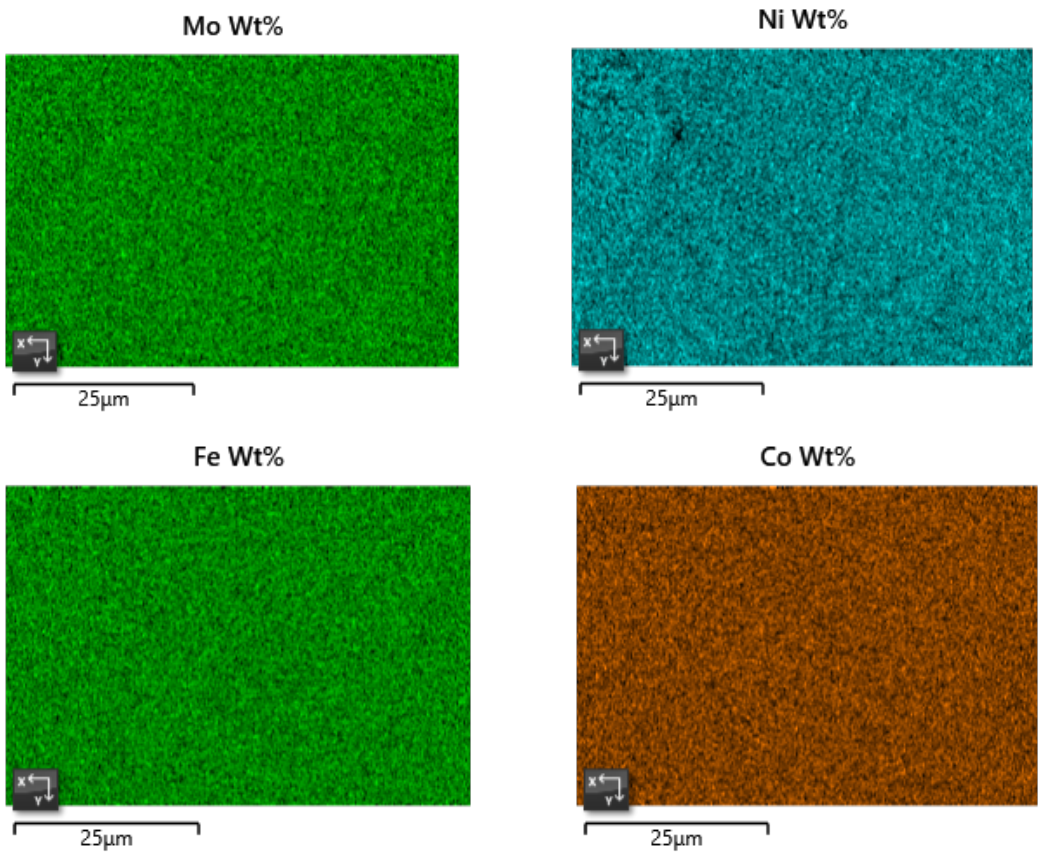


Figure 9 (DILAPRO Data). *Microstructure of the LPBF processed IN625 in the middle region of wall (BD is vertical): a, b) optical microscopy images of the as-printed microstructure; c) EBSD IPF map of the as-printed microstructure, d) corresponding KAM map of the as-printed microstructure.*

4. General conclusions

All studied materials (SS 316L, IN718 and IN625) can be processed via various additive manufacturing technologies (LPBF and DED, etc.) and nearly full density can be reached. Generally, LPBF results in finer microstructures in the additively manufactured materials, while DED led to somewhat coarser microstructures. The interior of grains typically shows cellular/dendritic structure. The finer microstructure of the LPBF samples results in higher tensile strength and lower tensile ductility of the LPBF processed materials compared to the WAAM and DED processed counterparts. These observations are related to higher cooling rates observed in the LPBF process compared to the DED process. In general, additively manufactured materials tend to show similar or better level of properties (Tables 3, 6 and 9) compared to their

Copyright © by DILAPRO All Rights Reserved | D2.2 – Database for thermal effects on microstructure and mechanical properties of DILAFACT materials

conventional counterparts manufactured via traditional technologies (Tables 2, 5 and 8). The aging treatment of the additively manufactured IN718 can significantly improve their tensile strength and reduce tensile ductility due to precipitation of the γ' and γ'' strengthening precipitates. Post heat treatments of all studied materials can significantly modify their microstructure and tensile properties depending on the applied heat treatment parameters.

The SS316L and IN625 manufactured via LPBF in the DILAPRO project are characterized by high quality. Both are nearly fully dense. Their tensile properties (Tables 3, 6 and 9) are similar or exceed those reported for their conventional counterparts (Tables 2, 5, and 8). A few microcracks detected in the SS 316L did not affect its high cycle fatigue resistance, while no microcracks were observed in the IN625.

5. Bibliography

1. ASTM A240. Standard Specification for Chromium and Chromium-Nickel Stainless Steel Plate, Sheet, and Strip for Pressure Vessels and for General Applications. November 2022.
2. AMS 5524. Steel, Corrosion and Heat-Resistant, Sheet, Strip and Plate 18Cr - 13Ni - 2.5Mo (SAE 30316) Solution Heat Treated. December 2020.
3. AMS 5507. Steel sheet, strip, and plate, corrosion and heat resistant 17Cr - 13Ni - 2.5Mo (316L). March 2019.
4. C.W Kovach. High Performance Stainless Steels. Nickel Institute. January 2002. https://nickelinstitute.org/media/1702/highperformancestainlesssteels_11021_.pdf
5. G. O. Barrionuevo, I. La Fé-Perdomo, E. Cáceres-Brito, and W. Navas-Pinto, "Tensile/Compressive Response of 316L Stainless Steel Fabricated by Additive Manufacturing," *Ingenius*, vol. 2024, no. 31, pp. 9–18, Jan. 2024, DOI: https://dialnet.unirioja.es/descarga/articulo/9263250.pdf
6. B. Voloskov, S. Evlashin, S. Dagesyan, S. Abaimov, I. Akhatov, and I. Sergeichev, "Very high cycle fatigue behavior of additively manufactured 316L stainless steel," *Materials*, vol. 13, no. 15, Aug. 2020, DOI: 10.3390/ma13153293.
7. M. Chepkoech, P. Omoniyi, G. Owolabi. Fatigue response of additive-manufactured 316L stainless steel. *Metals*. 14 (2024) 988.
8. I. Yadroitsev, P. Bertrand, I. Smurov, I. Yadroitsev, and M. Pavlov, "Mechanical properties of samples fabricated by selective laser melting." *14èmes Assises Européennes du Prototypage & Fabrication Rapide, 24-25 Juin 2009, Paris,* DOI: https://www.researchgate.net/publication/268183323

Copyright © by DILAPRO All Rights Reserved

9. M. Mallaiah, S. Thapliyal, and S. Chandra Bose, Eds., “Recent Advances in Additive Manufacturing”, *Volume 1*. in Lecture Notes in Mechanical Engineering. Singapore: Springer Nature Singapore, 2025. DOI: 10.1007/978-981-97-6016-9.
10. D. Gu and H. Chen, “Selective laser melting of high strength and toughness stainless steel parts: The roles of laser hatch style and part placement strategy,” *Materials Science and Engineering: A*, vol. 725, pp. 419–427, May 2018, DOI: 10.1016/J.MSEA.2018.04.046.
11. V.G. Smelov, A.V. Sotov, A.V. Agapovichev, and T.M. Tomilina, “Selective Laser Melting of Metal Powder of Steel 3161,” in *IOP Conference Series: Materials Science and Engineering*, Institute of Physics Publishing, Sep. 2016. DOI: 10.1088/1757-899X/142/1/012071.
12. D. Wang, C. Song, Y. Yang, and Y. Bai, “Investigation of crystal growth mechanism during selective laser melting and mechanical property characterization of 316L stainless steel parts,” *Mater Des*, vol. 100, pp. 291–299, Jun. 2016, DOI: 10.1016/J.MATDES.2016.03.111.
13. F. Abroug, A. Monnier, L. Arnaud, Y. Balcaen, and O. Dalverny, “High cycle fatigue strength of additively manufactured AISI 316L Stainless Steel parts joined by laser welding,” *Eng Fract Mech*, vol. 275, p. 108865, Nov. 2022, DOI: 10.1016/J.ENGFRACMECH.2022.108865.
14. N. Wawrzyniak, P.R. Provencher, M. Brochu, and M. Brochu, “Tensile properties of SS316L produced by LPBF: Influence of specimen dimensions and surface condition,” *Mater Charact*, vol. 203, p. 113117, Sep. 2023, DOI: 10.1016/J.MATCHAR.2023.113117.
15. X. Wang, J. A. Muñiz-Lerma, M. Attarian Shandiz, O. Sanchez-Mata, and M. Brochu, “Crystallographic-orientation-dependent tensile behaviours of stainless steel 316L fabricated by laser powder bed fusion,” *Materials Science and Engineering: A*, vol. 766, p. 138395, Oct. 2019, DOI: 10.1016/J.MSEA.2019.138395.
16. N. Wawrzyniak, P. R. Provencher, M. Brochu, and M. Brochu, “Tensile properties of SS316L produced by LPBF: Influence of specimen dimensions and surface condition,” *Mater Charact*, vol. 203, p. 113117, Sep. 2023, DOI: 10.1016/J.MATCHAR.2023.113117.
17. P. Kumar, R. Jayaraj, J. Suryawanshi, U. R. Satwik, J. McKinnell, and U. Ramamurty, “Fatigue strength of additively manufactured 316L austenitic stainless steel,” *Acta Mater*, vol. 199, pp. 225–239, Oct. 2020, DOI: 10.1016/J.ACTAMAT.2020.08.033.
18. N. D. Vallejo, C. Lucas, N. Ayers, K. Graydon, H. Hyer, and Y. Sohn, “Process optimization and microstructure analysis to understand laser powder bed fusion of 316L stainless steel,” *Metals (Basel)*, vol. 11, no. 5, May 2021, DOI: 10.3390/met11050832.
19. H. D. Carlton, A. Haboub, G. F. Gallegos, D. Y. Parkinson, and A. A. MacDowell, “Damage evolution and failure mechanisms in additively manufactured stainless steel,” *Materials Science and Engineering: A*, vol. 651, pp. 406–414, Jan. 2016, DOI: 10.1016/J.MSEA.2015.10.073.
20. X. Chen, J. Li, X. Cheng, B. He, H. Wang, and Z. Huang, “Microstructure and mechanical properties of the austenitic stainless steel 316L fabricated by gas metal arc additive

Copyright © by DILAPRO All Rights Reserved

manufacturing," *Materials Science and Engineering: A*, vol. 703, pp. 567–577, Aug. 2017, DOI: 10.1016/J.MSEA.2017.05.024.

21. C. M. Davies, H. Thomlinson, and P. A. Hooper, "Fatigue Crack Initiation and Growth Behavior of 316L Stainless Steel Manufactured Through Selective Laser Melting," *Proceedings of the ASME 2017 Pressure Vessels and Piping Conference*. *Volume 6A: Materials and Fabrication*. Waikoloa, Hawaii, USA. July 16–20, 2017, DOI: 10.1115/PVP2017-65410
22. T. M. Mower and M. J. Long, "Mechanical behavior of additive manufactured, powder-bed laser-fused materials," *Materials Science and Engineering: A*, vol. 651, pp. 198–213, Jan. 2016, DOI: 10.1016/J.MSEA.2015.10.068.
23. A. Riemer, S. Leuders, M. Thöne, H. A. Richard, T. Tröster, and T. Niendorf, "On the fatigue crack growth behavior in 316L stainless steel manufactured by selective laser melting," *Eng Fract Mech*, vol. 120, pp. 15–25, Apr. 2014, DOI: 10.1016/J.ENGFRACMECH.2014.03.008.
24. A. Yankin, A. Perveen, and D. Talamona, "Investigation and prediction of fatigue performance of SLM 316 L stainless steel based on small build orientation variations and heat treatment effects," *Sci Rep*, vol. 15, no. 1, Dec. 2025, DOI: 10.1038/s41598-025-89003-2.
25. Y. Chen, M. T. Chen, O. Zhao, B. Rossi, and X. Ruan, "Fatigue crack growth behavior of wire arc additively manufactured 316L austenitic stainless steel," *Thin-Walled Structures*, vol. 212, p. 113182, Jul. 2025, DOI: 10.1016/J.TWS.2025.113182.
26. W. Tang, D. Giuliano, O. Martinez, K. Banerjee, A. Nycz, M. Gussev, L. Meyer, and D. Vaughan "Stainless Steel Wire Arc Additive Manufacturing and Characterization for Potential SNF Canister Production," *In Proceedings of International High-Level Radioactive Waste Management Conference (IHLRWM)*, Phoenix, Arizona, United States of America - 11/13/2022.
27. A.B.Spierings, T.L. Starr, and K. Wegener, "Fatigue performance of additive manufactured metallic parts", *Rapid Prototyping Journal*, Vol. 19 No. 2, pp. 88-94, 2013. DOI: 10.1108/13552541311302932
28. M. Zhang et al., "Fatigue and fracture behaviour of laser powder bed fusion stainless steel 316L: Influence of processing parameters," *Materials Science and Engineering: A*, vol. 703, pp. 251–261, Aug. 2017, DOI: 10.1016/J.MSEA.2017.07.071.
29. M. Zhang, CN. Sun, X. Zhang, et al. "Elucidating the Relations Between Monotonic and Fatigue Properties of Laser Powder Bed Fusion Stainless Steel 316L", *JOM,* vol. 70, pp. 390–39, 2018. DOI: 10.1007/s11837-017-2640-z.
30. J. T. Pacheco et al., "Laser directed energy deposition of AISI 316L stainless steel: The effect of build direction on mechanical properties in as-built and heat-treated conditions,"

Copyright © by DILAPRO All Rights Reserved | D2.2 – Database for thermal effects on microstructure and mechanical properties of DILAFACT materials

Advances in Industrial and Manufacturing Engineering, vol. 4, p. 100079, May 2022, DOI: 10.1016/J.AIME.2022.100079.

31. B. Karan, M. Vadani, P. Muralishankar, K. Moheimani, A. Bhowmik, M. Zhang. Determining the necessity of post-processing heat treatment for the 316L stainless steel manufactured by LPBF through evaluation of mechanical and corrosion properties. *Advanced Engineering Materials*. 27 (2025) 2401442. DOI: 10.1002/adem.202401442.
32. K. Burdová , H. Jirková , L. Kučerová , I. Zetková , J. Mach. Effects of Heat Treatment on Additively Manufactured 316L Stainless Steel. *Manufacturing Technology.* 22 (2022) 261-266. DOI: 10.21062/mft.2022.042.
33. Y.H. Rajashilpage, R.A. Yildiz, M. Malekan. Effects of post-heat treatment on the mechanical properties of additive manufactured 316L stainless steel and Inconel 625 superalloy. *Procedia Structural Integrity*. 68 (2025) 981-987. DOI: 10.1016/j.prostr.2025.06.160.
34. Y. M. Wang *et al.*, "Additively manufactured hierarchical stainless steels with high strength and ductility", *Nat Mater*, vol. 17, nº 1, p. 63–70, Jan. 2018, DOI: 10.1038/NMAT5021.
35. J. Jeong, S. Webster, S. Liao, J.E. Mogonye, K. Ehmann, J. Cao. Cooling rate measurement in directed energy deposition using PDPT. *Additive Manufacturing Letters*. 3 (2022) 100101. DOI: 10.1016/j.addlet.2022.100101.
36. K. Kosiba, T. Gustmann, J.T. Kim, J. Seok, J. Jung, L. Beyer, S. Scudino, L. Giebeler, J. Han, K.J. Hufenbach. Experimental cooling rates during high-power LPBF at varying processing conditions. *Journal of Alloys and Compounds.* 967 (2023) 171773. DOI: 10.1016/j.jallcom.2023.171773.
37. UNS N07718. Standard Specification for Precipitation-Hardening Nickel Alloy Bars, Forgings, and Forging Stock for High-Temperature Service.
38. AMS 5662. ALLOY BARS, FORGINGS, AND RINGS, CORROSION AND HEAT RESISTANT Nickel Base - 19Cr - 3.1Mo - 5.1(Cb + Ta) - 0.90Ti - 0.50Al Consumable Electrode or Vacuum Induction Melted, Solution Treated. August 2022.
39. AMS 5664G. ALLOY BARS, FORGINGS, AND RINGS, CORROSION AND HEAT RESISTANT Nickel Base - 19Cr - 3.1Mo - 5.1(Cb + Ta) - 0.90Ti - 0.50Al Consumable Electrode Melted, Solution Treated at 1950 F (1065.6 C). August 2022.
40. AMS 5596 ALLOY SHEET, STRIP, AND PLATE, CORROSION AND HEAT RESISTANT Nickel Base - 19Cr - 3.1Mo - 5.2(Cb + Ta) - 0.90Ti - 0.60Al Consumable Electrode or Vacuum Induction Melted, Annealed. May 2023.
41. AMS 5597. ALLOY SHEET, STRIP, AND PLATE, CORROSION AND HEAT RESISTANT Nickel Base - 19Cr - 3.1Mo - 5.1(Cb + Ta) - 0.90Ti - 0.50Al Consumable Electrode Melted, Solution Treated at 1950 F (1065.6 C). April 2022.

Copyright © by DILAPRO All Rights Reserved | D2.2 – Database for thermal effects on microstructure and mechanical properties of DILAFACT materials

42. Q. Huan, “Review of IN 718 Alloy: Its History, Properties, Processing and Developing Substitutes,” *Journal of Materials Engineering*, vol. 8, pp. 92-100, 2012, https://jme.biam.ac.cn/EN/Y2012/V0/I8/92#2
43. E. Chlebus, K. Gruber, B. Kuźnicka, J. Kurzac, T. Kurzynowski. Effect of heat treatment on the microstructure and mechanical properties of Inconel 718 processed by selective laser melting. *Materials Science and Engineering A*. 639 (2015) 647-655. DOI: 10.1016/j.msea.2015.05.035.
44. A. Schmiedel, C. Burkhardt, S. Henkel, A. Weidner, and H. Biermann, “Very high cycle fatigue investigations on the fatigue strength of additive manufactured and conventionally wrought inconel 718 at 873 K,” *Metals (Basel)*, vol. 11, no. 11, Nov. 2021, DOI: 10.3390/met11111682.
45. F. Uriati, G. Nicoletto, and A. H. A. Lutey, “As-built surface quality and fatigue resistance of Inconel 718 obtained by additive manufacturing,” *Material Design and Processing Communications*, vol. 3, no. 4, Aug. 2021, DOI: 10.1002/mdp2.228.
46. Y. N. Zhang, X. Cao, P. Wanjara, and M. Medraj, “Tensile properties of laser additive manufactured Inconel 718 using filler wire,” *J Mater Res*, vol. 30, no. 4, pp. 2006–2020, Aug. 2015, DOI: 10.1557/jmr.2014.199.
47. S. Heo, Y. Lim, N. Kwak, C. Jeon, M. Choi, and I. Jo, “Impact of Heat Treatment and Building Direction on Tensile Properties and Fracture Mechanism of Inconel 718 Produced by SLM Process,” *Metals (Basel)*, vol. 14, no. 4, Apr. 2024, DOI: 10.3390/met14040440.
48. T. Zhang, H. Li, H. Gong, Y. Wu, A. S. Ahmad, and X. Chen, “Effect of rolling force on tensile properties of additively manufactured Inconel 718 at ambient and elevated temperatures,” *J Alloys Compd*, vol. 884, Dec. 2021, DOI: 10.1016/j.jallcom.2021.161050.
49. S. Choudhary, A. Pandey, and V. Gaur, “Role of microstructural phases in enhanced mechanical properties of additively manufactured IN718 alloy,” *Materials Science and Engineering: A*, vol. 862, p. 144484, Jan. 2023, DOI: 10.1016/J.MSEA.2022.144484.
50. M. Ni *et al.*, “Anisotropic tensile behavior of in situ precipitation strengthened Inconel 718 fabricated by additive manufacturing,” *Materials Science and Engineering: A*, vol. 701, pp. 344–351, Jul. 2017, DOI: 10.1016/J.MSEA.2017.06.098.
51. M. E. Aydinöz *et al.*, “On the microstructural and mechanical properties of post-treated additively manufactured Inconel 718 superalloy under quasi-static and cyclic loading,” *Materials Science and Engineering: A*, vol. 669, pp. 246–258, Jul. 2016, DOI: 10.1016/J.MSEA.2016.05.089.
52. S. H. Sun *et al.*, “Electron beam additive manufacturing of Inconel 718 alloy rods: Impact of build direction on microstructure and high-temperature tensile properties,” *Addit Manuf*, vol. 23, pp. 457–470, Oct. 2018, DOI: 10.1016/J.ADDMA.2018.08.017.
53. K. Moussaoui, W. Rubio, M. Mousseigne, T. Sultan, and F. Rezai, “Effects of Selective Laser Melting additive manufacturing parameters of Inconel 718 on porosity, microstructure

Copyright © by DILAPRO All Rights Reserved | D2.2 – Database for thermal effects on microstructure and mechanical properties of DILAFACT materials

and mechanical properties," *Materials Science and Engineering: A*, vol. 735, pp. 182–190, Sep. 2018, DOI: 10.1016/J.MSEA.2018.08.037.

54. K. Gruber, W. Stopyra, K. Kobiela, B. Madejski, M. Malicki, and T. Kurzynowski, "Mechanical properties of Inconel 718 additively manufactured by laser powder bed fusion after industrial high-temperature heat treatment," *J Manuf Process*, vol. 73, pp. 642–659, Jan. 2022, DOI: 10.1016/J.JMAPRO.2021.11.053.
55. E. Hosseini and V. A. Popovich, "A review of mechanical properties of additively manufactured Inconel 718," *Addit Manuf*, vol. 30, p. 100877, Dec. 2019, DOI: 10.1016/J.ADDMA.2019.100877.
56. Y. Wang, et al. "Defects, microstructure, and properties in laser powder bed fusion IN718: Power density effects and feature maps," *Journal of Manufacturing Processes*. Vol. 135, pp. 240-252, 2025, DOI: 10.1016/j.jmapro.2025.01.
57. C. E. Seow, H. E. Coules, G. Wu, R. H. U. Khan, X. Xu, and S. Williams, "Wire + Arc Additively Manufactured Inconel 718: Effect of post-deposition heat treatments on microstructure and tensile properties," *Mater Des*, vol. 183, Dec. 2019, DOI: 10.1016/j.matdes.2019.108157.
58. AMS 5599. Alloy sheet, strip, plate, corrosion and heat resistant Nickel Base - 21.5Cr - 9.0Mo - 3.7(Cb + Ta). July 2022.
59. AMS 5666. Alloy bars, forgings, and rings, corrosion and heat resistant Nickel Base - 21.5Cr - 9.0Mo - 3.7(Cb + Ta). July 2022.
60. ASTM B446. Standard Specification for Nickel-Chromium-Molybdenum-Columbium Alloy (UNS N06625), Nickel-Chromium-Molybdenum-Silicon Alloy (UNS N06219), and Nickel-Chromium-Molybdenum-Tungsten Alloy (UNS N06650) Rod and Bar.
61. ASTM B443. Standard Specification for Nickel-Chromium-Molybdenum-Columbium Alloy and Nickel-Chromium-Molybdenum-Silicon Alloy Plate, Sheet, and Strip. November 2019.
62. UNS N06625. Corrosion-resistance and heat-resistant Nickel Alloy.
63. J. B. Singh, "Materials Horizons: From Nature to Nanomaterials Alloy 625 Microstructure, Properties and Performance." Springer, 2022, DOI: 10.1007/978-981-19-1562-8.
64. F. Xu, Y. Lv, Y. Liu, F. Shu, P. He, and B. Xu, "Microstructural Evolution and Mechanical Properties of Inconel 625 Alloy during Pulsed Plasma Arc Deposition Process," *J Mater Sci Technol*, vol. 29, no. 5, pp. 480–488, May 2013, DOI: 10.1016/J.JMST.2013.02.010.
65. F. Concli, R. Gerosa, D. Panzeri, and L. Fraccaroli, "High- and low-cycle-fatigue properties of additively manufactured Inconel 625," *Progress in Additive Manufacturing*, Dec. 2024, DOI: 10.1007/s40964-023-00545-1.
66. N. Martin, A. Hor, E. Copin, P. Lours, and L. Ratsifandrihana, "Fatigue properties of as-built and heat-treated Inconel 625 obtained by the hybridization of two laser-powder based additive processes," *Int J Fatigue*, vol. 172, p. 107650, Jul. 2023, DOI: 10.1016/J.IJFATIGUE.2023.107650.

Copyright © by DILAPRO All Rights Reserved

67. J. Lee *et al.*, “Enhancement of tensile properties and isotropy of wire arc additive manufactured alloy 625 via thermomechanical process,” *Mater Today Commun*, vol. 40, p. 109349, Aug. 2024, DOI: 10.1016/J.MTCOMM.2024.109349.
68. F. Chen, Q. Wang, C. Zhang, Z. Huang, M. Jia, and Q. Shen, “Microstructures and mechanical behaviors of additive manufactured Inconel 625 alloys via selective laser melting and laser engineered net shaping,” *J Alloys Compd*, vol. 917, p. 165572, Oct. 2022, DOI: 10.1016/J.JALLCOM.2022.165572.
69. G. Marchese, G. Piscopo, S. Lerda, A. Salmi, E. Atzeni, and S. Biamino, “Heat-Treated Inconel 625 by Laser Powder Bed Fusion: Microstructure, Tensile Properties, and Residual Stress Evolution,” *J Mater Eng Perform*, vol. 33, DOI: 10.1007/s11665-02.
70. S. K. Nayak, S. K. Mishra, A. N. Jinoop, C. P. Paul, and K. S. Bindra, “Experimental Studies on Laser Additive Manufacturing of Inconel-625 Structures Using Powder Bed Fusion at 100 µm Layer Thickness,” *J Mater Eng Perform*, vol. 29, no. 11, pp. 7636–7647, Nov. 2020, DOI: 10.1007/s11665-020-05215-9.
71. C. P. Paul, P. Ganesh, S. K. Mishra, P. Bhargava, J. Negi, and A. K. Nath, “Investigating laser rapid manufacturing for Inconel-625 components,” *Opt Laser Technol*, vol. 39, no. 4, pp. 800–805, Jun. 2007, DOI: 10.1016/J.OPTLASTEC.2006.01.008.
72. S. Sui *et al.*, “Additive manufacturing of ultrastrong and ductile nickel matrix composites via hetero-deformation induced strengthening,” *International Journal of Extreme Manufacturing*, vol. 7, no. 4, Aug. 2025, DOI: 10.1088/2631-7990/adbb32.
73. Q. Yang, Y. Wu, F. Sha, “Microstructure and mechanical properties of Inconel 625 alloy manufactured by selective laser melting”, *Mater. Mech. Eng.* 2016, *40*, 83–87.
74. H. Wong, K. Dawson, G.A. Ravi, L. Howlett, R.O. Jones, C.J. Sutcliffe, “Multi-laser powder bed fusion benchmarking—Initial trials with Inconel 625”, *Int. J. Adv. Manuf. Technol.* 2019, *105*, 2891–2906, DOI: 10.1007/s00170-019-04417-3.
75. P. Wang, B. Zhang, C.C. Tan, S. Raghavan, Y.F Lim, C. N. Sun, J. Wei, D. Chi, “Microstructural characteristics and mechanical properties of carbon nanotube reinforced Inconel 625 parts fabricated by selective laser melting. *Mater. Des.* 2016, *112*, 290–299, DOI: 10.1016/j.matdes.2016.09.080
76. M. R. Stoudt et al., “Location-Specific Microstructure Characterization Within IN625 Additive Manufacturing Benchmark Test Artifacts”, *Integrating Materials and Manufacturing Innovation* (2020) 9:54–69, DOI: 10.1007/s40192-020-00172-6
77. G. Kishor, K.K. Mugada, R.P. Mahto, A. Sivanandam, D.R. Kumar, and M. Amirthalingam, “Effect of Crystallographic Texture and Grain Orientation on Tribological Properties of WAAM Deposited IN625 Alloy in Weaving Deposition Strategy”, *Materials Chemistry and Physics*, Vol. 329, p. 130089, 2025, DOI: 10.1016/j.matchemphys.2024.130089.

Copyright © by DILAPRO All Rights Reserved | D2.2 – Database for thermal effects on microstructure and mechanical properties of DILAFACT materials